Cellulose (2024) 31:9715–9729
https://doi.org/10.1007/s10570-024-06193-0

ORIGINAL RESEARCH

Mechanical, thermal, and morphological properties of nanocellulose reinforced ABS nanocomposites

Sultan Çavdar · Harun Sepetcioglu · İdris Karagöz

Received: 17 May 2024 / Accepted: 24 September 2024 / Published online: 5 October 2024

Abstract This study provides a comprehensive analysis of the effects of incorporating low levels of cellulose nanofibrils (CNFs) into an acrylonitrile butadiene styrene (ABS) matrix on the properties of ABS composites. Five samples with varying CNF content (0.125%, 0.25%, 0.5%, and 1%) were prepared, alongside a pure ABS sample for comparison. The preparation involved mechanical blending, followed by extrusion and injection molding. Mechanical, thermal, water absorption, surface gloss, and microstructural properties of the composites were characterized. Tensile and three-point bending tests revealed that the addition of CNFs improved both stiffness and strength, with the highest tensile modulus observed in ABS/NC4 (1% CNFs) and the highest flexural strength in ABS/NC1 (0.125% CNFs). Impact resistance, evaluated through Charpy impact testing, showed enhancement up to 0.5% CNF content, beyond which a decline was observed due to increased particle quantity. Thermal properties exhibited negligible changes, with slight variations in glass transition and melting temperatures observed within a narrow range. SEM analysis confirmed a uniform distribution of CNFs, contributing to enhanced crack resistance, although higher CNF content led to increased void formation. Surface gloss measurements indicated smoother material surfaces with higher CNF content. The study concludes that integrating CNFs into ABS composites improves mechanical properties and impact resistance, necessitating careful consideration of CNF content for optimal performance. Further refinement could tailor ABS/CNF composites for specific applications.

Keywords Acrylonitrile butadiene styrene · Cellulose nanofibrils · Composites · Nanocellulose · Nanocomposites

S. Çavdar · H. Sepetcioglu (✉)
Department of Metallurgical and Materials Engineering, Institute of Sciences, Selçuk University, 42075 Konya, Türkiye
e-mail: harunsepet@selcuk.edu.tr

İ. Karagöz (✉)
Department of Polymer Materials Engineering, Faculty of Engineering, Yalova University, 77200 Yalova, Türkiye
e-mail: idris.karagoz@yalova.edu.tr

Introduction

Nanocelluloses, renowned for their biodegradable and biocompatible properties, are innovative materials gaining attention due to their growing utilization in industrial applications. The nanocellulose family comprises cellulose nanofibrils (CNFs), cellulose nanocrystals (CNCs), and bacterial nanocellulose (BNC), each distinguished by their sources, production techniques, structural attributes, and properties (Farooq et al. 2020).

CNFs have attracted considerable interest among scientists and engineers due to their renewable and

sustainable nature. CNFs can be obtained through bottom-up biosynthesis by bacteria or top-down disintegration of plant materials. They have been extensively studied and reviewed, with significant advancements reported in their production and applications across various fields such as tissue engineering, biomedical engineering, and advanced fiber composites (Lee et al. 2014). The synthetic polymer-compatible properties of CNFs make them highly desirable for a wide range of industrial applications, including biomedical products (Farooq et al. 2020), packaging materials (Wang et al. 2022), paper and board coatings (Tozluoglu et al. 2022), textiles (Jenol et al. 2022), films (Boufi et al. 2014), food packaging and additives (Zhang et. al 2021), energy storage devices (Guo et al. 2020), sensors (Misenan et al. 2022), hydrogels, and implants (Zaaba et al. 2021).

Studies on the production and usability of nanocellulose-reinforced nanocomposites have been ongoing for a significant period. Particularly in the last decade, researcher interest in this topic has intensified. The initial research in 1987 aimed to explore the reinforcement potential of cellulose in polymers such as polypropylene, polystyrene, and high-density polyethylene (Boldizar et al. 1987). This foundational study was followed by subsequent research that further highlighted the significant reinforcing capabilities of nanocellulose. Subsequent studies (Favier et al. 1995a, 1995b) have shown that low loading of nanocellulose significantly improves the mechanical properties of nanocomposites by forming a rigid whisker network via percolation. These enhanced nanocomposites offer numerous benefits, including affordability, lightweight construction, renewability, energy efficiency, distinctive properties, biodegradability, and the reactive surface characteristics of nanocellulose. Additionally, nanocomposites with desired hardness and flexibility can be tailored using CNFs with different mechanical properties (Kargarzadeh et al. 2017, 2018).

Leão et al. (2020) investigated the reinforcement of acrylonitrile–butadiene–styrene (ABS) with cellulose nanocrystals derived from sugarcane bagasse. They focused on variations in mechanical and thermal performance and found that incorporating up to 0.5% cellulose nanocrystals significantly enhanced impact strength, elastic modulus, storage modulus, and viscosity, while compromising tensile strength and thermal stability. However, exceeding 0.5% nanocrystal content resulted in a decrease in the properties of the nanocomposites (Leao et al. 2020). Diaz de León et al. (2021) examined how modified nanocrystals affected ABS nanocomposites, revealing improved Young's modulus and yield strength at a concentration of 1 wt.%, despite a decline in impact strength due to heightened stiffness. Remarkably, they found that the incorporation of cellulose nanocrystals did not affect the glass transition temperature of ABS (Díaz de León et al. 2021). Feng et al. (2017) utilized lignin-coated cellulose nanocrystals (L-CNCs) to reinforce 3D printed ABS, resulting in reduced density and increased tensile and storage modulus upon the addition of 4% L-CNCs. Additionally, enhanced thermal stability and effective dispersion and interfacial adhesion between L-CNCs and ABS were noted, indicating potential applications in lightweight and rigid end-use products (Feng et al. 2017).

To the best of the authors' knowledge, CNCs have been widely utilized in the production of nanocomposites, particularly those based on ABS (Moon et al. 2011; Siró and Plackett 2010). However, there remains a notable gap in the literature regarding the comprehensive exploration of CNFs in reinforced ABS nanocomposites. Existing publications have primarily focused on the utilization of CNFs in various composite formulations, but discussions specifically addressing their integration into the ABS matrix are lacking. To address this research gap, the present study conducts a comparative analysis to investigate the effects of CNFs on the properties of ABS nanocomposites. The primary aim of this study is twofold: firstly, to evaluate the enhancements in thermal, mechanical, and water absorption properties resulting from the integration of a biobased reinforcement with an ABS matrix; secondly, to scrutinize the reinforcing efficiency of CNFs with a comprehensive overview. This research aims to contribute to the understanding of sustainable materials development and the potential of bio-based composites in sectors such as automotive, electronics, packaging, construction, and sports equipment.

Materials and methods

Materials

In the preparation of ABS/CNF composites, ABS 750SW, a commercial-grade ABS raw material with a density of 1.04 g/cm^3 and a Melt Flow Index (MFI) value of 38 g/10 min, sourced from Kumko Petrochemical, was utilized as the matrix material. CNFs, with a diameter of 10–20 nm, a length of 2–3 µm, a density of 1.50 g/cm^3, and a crystallinity ratio of 92%, obtained from Nanografi company, were employed as the additive material.

Preparation of ABS/CNF composites and test samples

Initially, ABS and CNFs were added to a bucket and subjected to a mechanical blending process for 10 min. After blending, the samples were extruded into filament form using an extruder machine equipped with a special mixing screw from the Robodigg brand, employing the melt blending method. The temperature profile during the extrusion process was set to 25/60/160/180 °C. The extruder screw had a diameter of Ø25 mm, a screw speed of 1300 RPM, and a torque of 20 Nm. The length-to-diameter (L/D) ratio of the screw was 16. Subsequently, the ABS/CNF composite filaments were granulated with the assistance of a granulator. The ABS/CNF material in granular form was dried at 80 °C for 2 h in a Binder brand oven to remove moisture before the injection process. Test specimens compliant with ISO 294 standards were produced by injection molding from the granule-form mixtures using the Spex 400 model injection machine from the Engel company. The molding parameters were set at 80 bar injection pressure, 50 mm/s injection speed, 55 bar holding pressure, and a 30-s cycle time. Five samples were prepared, including pure ABS, by adding CNFs to ABS at ratios of 0.125%, 0.25%, 0.5%, and 1%. The formulations of ABS/CNF composites, which contain ABS and CNF, are presented in Table 1. A schematic representation of the entire process, from production to characterization of ABS/CNF composites, is provided in Fig. 1.

Table 1 The formulations details and codes of ABS/CNF composites

Sample codes	ABS (wt.%)	CNF (wt.%)	Prepared mixture amount (g)
ABS/NC0	100	–	3000
ABS/NC1	99.875	0.125	3000
ABS/NC2	99.75	0.25	3000
ABS/NC3	99.50	0.50	3000
ABS/NC4	99	1	3000

Characterization

The tensile test and the three-point bending test were performed at room temperature using a Zwick Z020 Model testing machine equipped with a 20 kN load cell. The tensile test followed the ISO 527–1 standard with a rosshead speed of 50 mm/min, while the three-point bending test adhered to the ISO 178 standard with a bending rate of 1.7 mm/min using a compression fixture. Both tests were conducted on 5 specimens each, and the average results were calculated. Charpy impact testing, following ISO 180, was conducted using a 7.5 J hammer on an Instron 120D Model testing machine. For both notched and unnotched impact tests, 10 specimens were used, and the average results were calculated. Hardness measurements were carried out according to the ISO 48–4 standard using the Shore D scale, employing a Loyka M01D brand analog durometer. Ten readings were taken for each sample, and the Shore D hardness value was determined by calculating the average of these measurements.

The density of ABS/CNF composites was determined following the liquid pycnometer method (Karagöz 2024) outlined in ISO 1183. Three replicates were performed, and the average result was calculated. The initial weights of samples, cut into rectangular shapes with dimensions of 4×20x30 mm for the water absorption test, were measured to establish their initial weight. Subsequently, the samples were fully immersed in water within the test container to undergo the water absorption process. After the initial one-hour period, the materials were carefully removed from the container using tweezers. Excess water on the sample surfaces was then gently removed by drying with paper towels without

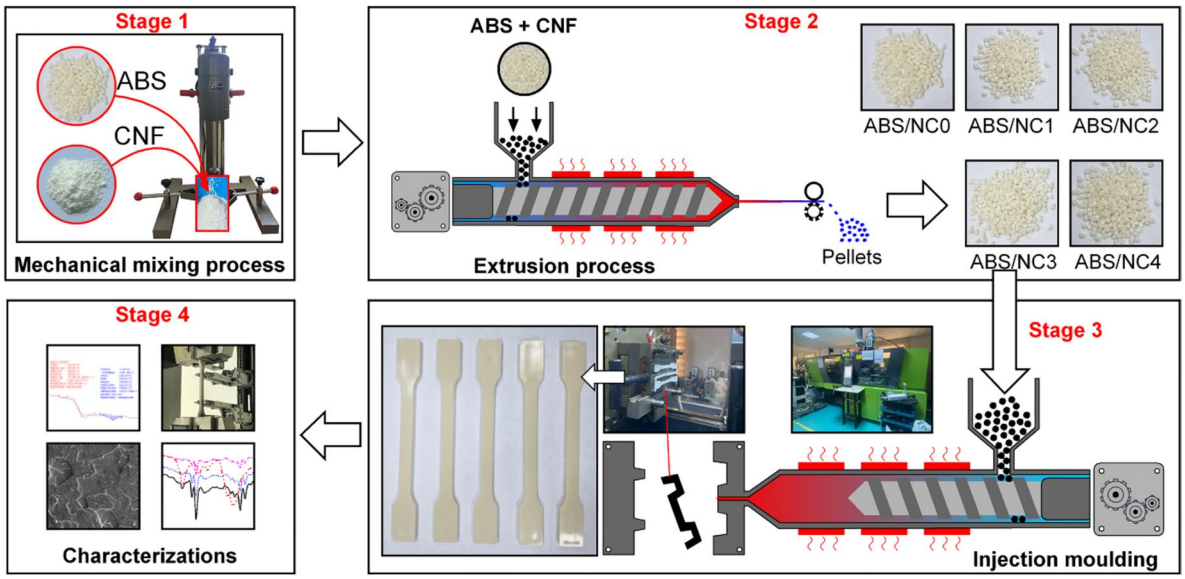

Fig. 1 Schematic representation of the entire process from production to characterization of ABS/CNF composites

applying pressure. The samples were subsequently reweighed, and the amount of water absorption capacity (WAC) was calculated using the equation provided in Eq. 1 below. These measurements were initially taken after a one-hour period. Subsequently, they were repeated at different time intervals over a span of 744 h. The test was conducted with 5 specimens, each with replicates.

$$\mathrm{WAC} = \left(\frac{Final\,weight - Inital\,weight}{Initalweight} \right) \times 100 \quad (1)$$

Surface gloss measurements were conducted using an Elcometer micro-gloss device at a 60° projection angle, following ASTM D523 standards. Measurements were performed in replicates of 5, and the average was calculated. FT-IR tests were conducted on a Perkin Elmer Spectrum 100 FT-IR instrument, following the ASTM D6348 standard, covering the wavelength range from 4000 to 400 cm^{-1}. To observe the thermal transitions of ABS/CNF composites, thermal properties were examined using differential scanning calorimetry (DSC, Mettler Toledo TGA/DSC2 Star System) according to the ASTM D3417 standard. The heating rate was set at 10 °C/min under a nitrogen atmosphere. Thermogravimetric analysis (TGA) was performed using a Seiko Exstar TG/DTA 6300 instrument under a nitrogen flow. The ABS/CNF composite samples were heated up to 600 °C at a heating rate of 10 °C/min. FT-IR, DSC, and TGA tests were conducted on a single specimen. The morphology of the fractured surfaces of materials obtained from the impact test was examined using the Zeiss Evo LS10 model scanning electron microscope (SEM). Prior to imaging, the samples were coated with a 100 Å gold layer under vacuum conditions to achieve an inert and conductive surface. Microstructure images were captured using a voltage of 20 kV.

Results and discussion

Tensile and three-point bending test results of ABS/CNF composites

The tensile testing and three-point bending test results are summarized in Table 2, with a graphical representation of the tensile test outcomes depicted in Fig. 2a and the three-point bending test outcomes illustrated in Fig. 2b. ABS/CNF composites demonstrate an efficient process under tensile stress, characterized by plastic deformation followed by strain hardening. The highest tensile modulus, measured at 1013 ± 14 MPa, was achieved in sample ABS/NC4 with a CNF ratio of 1%. Lower CNF additions (0.125%, 0.25%, and

Table 2 The tensile and three-point bending test results

Sample codes	Tensile properties			Flexural properties		
	Tensile modulus (MPa)	Tensile strength (MPa)	Elongation at break (%)	Flexural modulus (MPa)	Flexural strength (MPa)	Flexural strain (mm/mm)
ABS/NC0	962 ± 10	42.2 ± 0.39	21 ± 4.40	3155 ± 66	98.4 ± 2.17	18.9 ± 5.07
ABS/NC1	992 ± 16	43.4 ± 0.94	9 ± 1.32	3026 ± 276	101.5 ± 1.20	11.9 ± 7.15
ABS/NC2	968 ± 20	41.8 ± 0.21	19 ± 3.11	3128 ± 52	98.9 ± 1.50	26.3 ± 2.05
ABS/NC3	980 ± 10	43.3 ± 0.32	18 ± 1.58	3134 ± 4	99.2 ± 1.27	28.0 ± 1.75
ABS/NC4	1013 ± 14	40.8 ± 0.19	11 ± 1.02	3139 ± 58	98.4 ± 2.83	6.8 ± 0.54

The values presented in the table are based on experimental testing and represent the average of multiple measurements

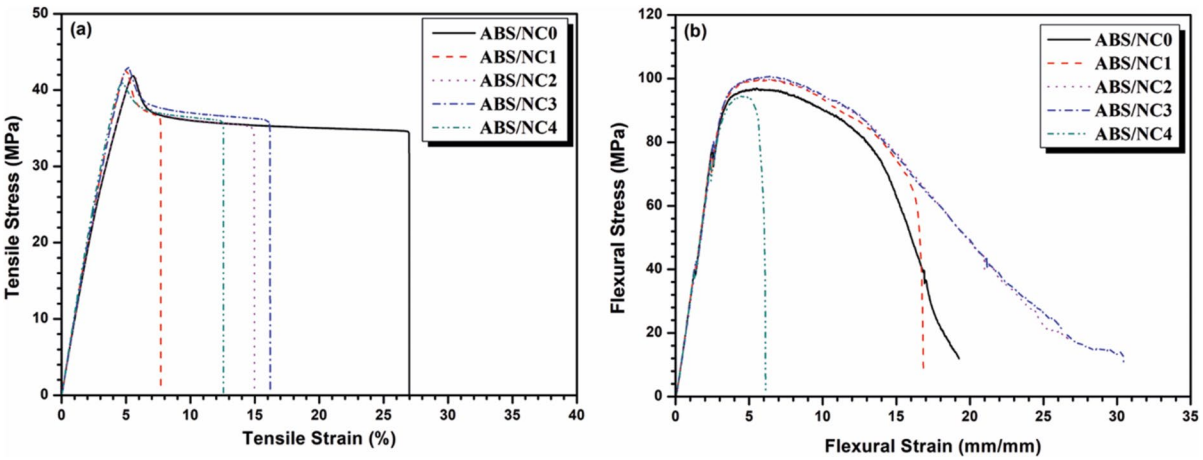

Fig. 2 Graphical comparison of tensile and three-point bending test results for ABS/CNF composites: **a** Tensile test results, **b** Flexural test results

0.5%) did not notably enhance tensile properties due to amorphous structure of ABS, whereas the addition of 1% CNF resulted in a slight increase in the tensile modulus (~3%) compared to others. It can be inferred that CNFs have a limited effect on tensile strength at low contribution rates. Consistent with prior research (Ma et al. 2015, 2017; Kargarzadeh et al. 2018; Souza et al. 2020) higher rates of CNF addition have been observed to positively influence the tensile properties of ABS while reducing elongation at break. It is expected that higher rates of CNF addition and the use of compatibilizers will further improve the tensile properties of ABS/CNF composites (Yang and Gardner 2011). The influence of CNFs in varying ratios from 0.125 to 1% on the flexural modulus is not substantial. Although the highest flexural strength, measured at 101.5 ± 1.20 MPa, was obtained in sample ABS/NC1 with a CNF ratio of 0.125%, it was not significantly higher compared to pure ABS (within the standard deviation). For other contribution ratios (between 0.25 and 1%), the flexural strength was comparable to that of pure ABS (ABS/NC0). During tensile testing, stresses are uniformly distributed across the cross-section, whereas in bending tests, they vary from zero in the middle to maximum at the top and bottom surfaces. The bending properties reflect any material heterogeneity and anisotropy. The slight discrepancies observed in bending test results may be attributed to such characteristics (Katagiri et al. 2023).

Charpy impact test results of ABS/CNF composites

The results of notched and unnotched Charpy impact tests for ABS/CNF composites are illustrated in Fig. 3. The unnotched impact strength of pure ABS

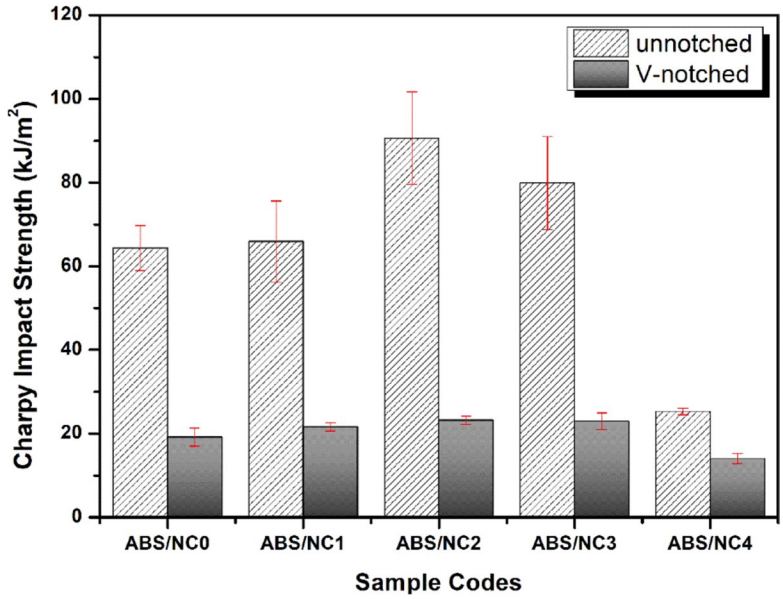

Fig. 3 Graphical comparison of Charpy impact test results for ABS/CNF composites

is measured at 64 kJ/m^2, while the notched impact strength is 19.2 kJ/m^2. The highest impact strength is attained in sample ABS/NC2 with a CNF content of 0.25%, showing an unnotched impact strength of 90.63 kJ/m^2 and a notched impact strength of 23.22 kJ/m^2. It can be observed that CNF content enhances impact strength up to 0.5% for both notched and unnotched Charpy impact tests. This improvement is explained by the increased energy absorption associated with higher CNF content (Saba et al. 2017; Katagiri et al. 2023). However, a decrease in impact strength is noted at CNF contents above 0.5%. This reduction may be attributed to the increased particle quantity, which could lead to reduced homogeneity within the composite. The higher particle content may introduce more defects and weak areas, resulting in the formation of microcracks and their accelerated propagation (Saba et al. 2017).

Hardness and density measurement results of ABS/CNF composites

The hardness and density measurement results of ABS/CNF composites are depicted in Fig. 4. When comparing the hardness measurement results, it was observed that the addition of CNFs in the range of 0.125% to 1% did not significantly affect the hardness of ABS/CNF composites. The absence of a regular crystal structure in ABS and the freer molecular movements may have contributed to the similar levels of hardness across different ratios (Bose et al. 2009; Saba et al. 2017). The slight differences in hardness among ABS/CNF composites could be attributed to the presence of CNFs at the measurement point, which restricts molecular movement (Saba et al. 2017).

The addition of CNF increased the density of ABS/CNF composites as expected. Specifically, the addition of 0.125% CNF increased the density of ABS by 0.19%, 0.25% CNFs increased it by 0.38%, 0.50% CNF by 0.77%, and 1.0% CNF by 1.44%. Density increases proportionally with the amount of CNF added as filler, indicating even distribution within the structure. The higher density of CNF compared to ABS, along with the increasing CNF ratio in the formulation, contributed to this density increase (Karagöz 2024; Mutlu et al. 2024).

Water absorption test results of ABS/CNF composites

The WAC results are presented in Fig. 5. Generally, both pure ABS and ABS/CNF composites exhibit low WAC. However, when compared internally, the water absorption capacity of all composites, except for the ABS/NC4 composite with 1% CNF, is lower than that of pure ABS. The ABS/NC4 composite exhibits a higher water absorption capacity compared to other

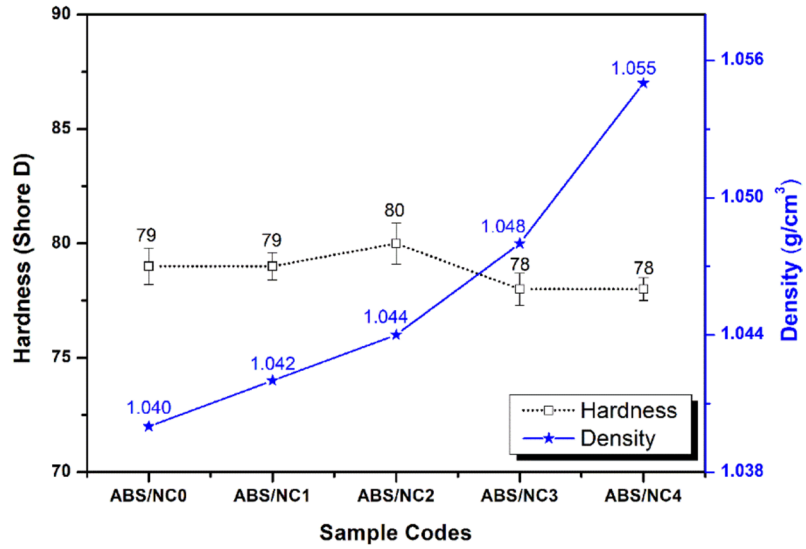

Fig. 4 Graphical comparison of hardness and density measurement results for ABS/CNF composites

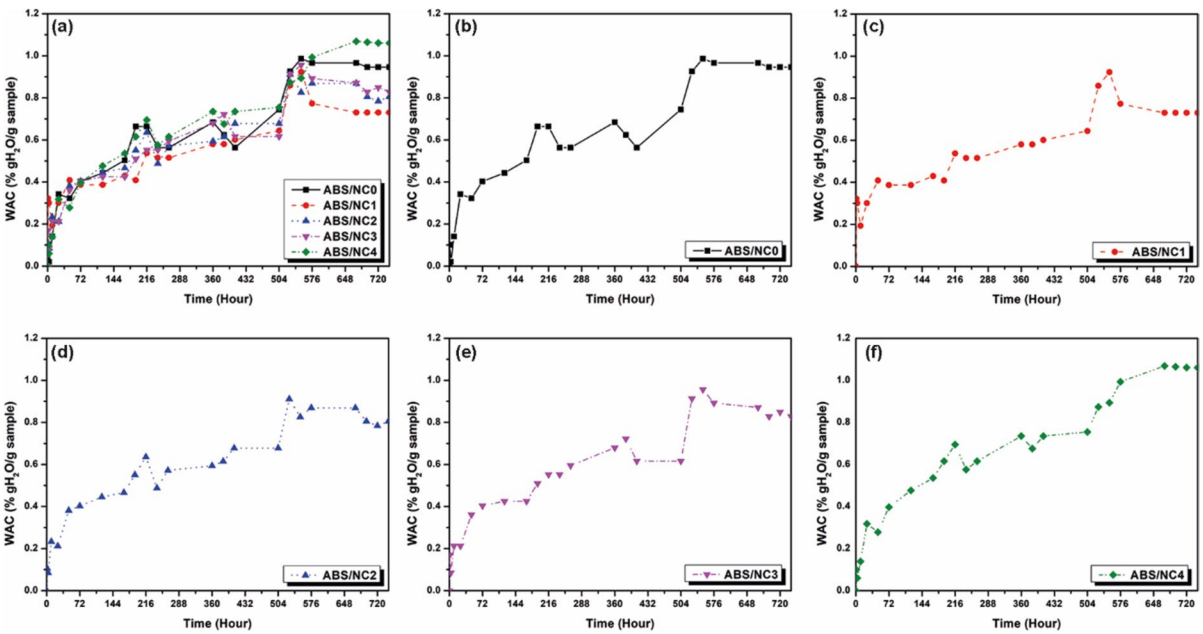

Fig. 5 Graphical comparison of water absorption capacity: **a** All ABS/CNF composites, **b** ABS/NC0, **c** ABS/NC1, **d** ABS/NC2, **e** ABS/NC3, **f** ABS/NC4

composites and pure ABS. This is believed to be due to the increasing hemicellulose content in the structure, as well as the good network stability and rebound properties of CNFs after compression (Kim et al. 2015; Karagöz et al. 2024). Except for the ABS/NC4 composite, it is observed that the initially high-water absorption capacity in all other ABS/CNF composites starts to decrease after 576 h. This indicates that the composites have reached their maximum moisture saturation level. For the ABS/NC4 composite, it is observed that the moisture saturation level is reached after 648 h.

Surface gloss measurement results of ABS/CNF composites

The surface gloss measurement results of ABS/CNF composites are presented in Table 3. The observed increases in gloss levels in ABS/CNF composites compared to pure ABS suggest that the presence of CNF enhances the surface gloss of the ABS matrix. Specifically, the higher gloss value obtained in the ABS/NC4 sample indicates the potential of CNF to improve the surface quality of the composite. These findings imply that optimizing the CNF content during production can enhance surface gloss in plastic composites where it is crucial, thereby meeting aesthetic expectations.

The increase in surface gloss with higher CNF content suggests that CNFs are uniformly dispersed within ABS. This is attributed to the homogeneous distribution of CNFs, which enhances surface smoothness and contributes to a smoother appearance of the material surface. Additionally, the naturally high reflectance properties of CNF further enhance the gloss level by promoting increased light reflection on the material surface (Ozcan et al. 2021; Spagnuolo et al. 2022).

Table 3 Surface gloss measurement results

Sample Codes	Surface Gloss (GU 60°)	Gloss Improved. Efficiency (%)	Gloss Class
ABS/NC0	61 (±1.3)	–	Semi-gloss
ABS/NC1	66 (±2.2)	+8.20	Semi-gloss
ABS/NC2	69 (±3.6)	+13.11	Semi-gloss
ABS/NC3	70 (±2.4)	+14.75	Semi-gloss
ABS/NC4	73 (±3.4)	+19.67	Glossy

FT-IR test results of ABS/CNF composites

The FT-IR results are presented in Fig. 6. In Fig. 6a, peaks obtained from the FT-IR analysis are shown individually, while in Fig. 6b displays overlapped. In the FT-IR analysis of ABS, wave numbers of 2920 cm^{-1} and 2851 cm^{-1} indicate the symmetric and asymmetric stretching vibrations of the methylene ($-CH_2-$) group, respectively. The wave number 2236 cm^{-1} represents the stretching vibration peak of the nitrile (-CN) group originating from the acrylonitrile component of the polymer, while 1599 cm^{-1} corresponds to the stretching vibration peak of the aryl group from the acrylonitrile component (Zhang et al. 2020; Qu et al. 2021). The wave number 1493 cm^{-1} reflects the bending vibration of the phenyl group. Bending vibrations of the phenyl group in the styrene component are observed at 1448 cm^{-1} and 1068 cm^{-1}, whereas the bending vibration of the aryl group of the acrylonitrile component appears at 1025 cm^{-1}. Outward bending vibrations of the phenyl ring in the styrene component are observed at wave numbers 758 cm^{-1} and 698 cm^{-1} (Afrin et al. 2022).

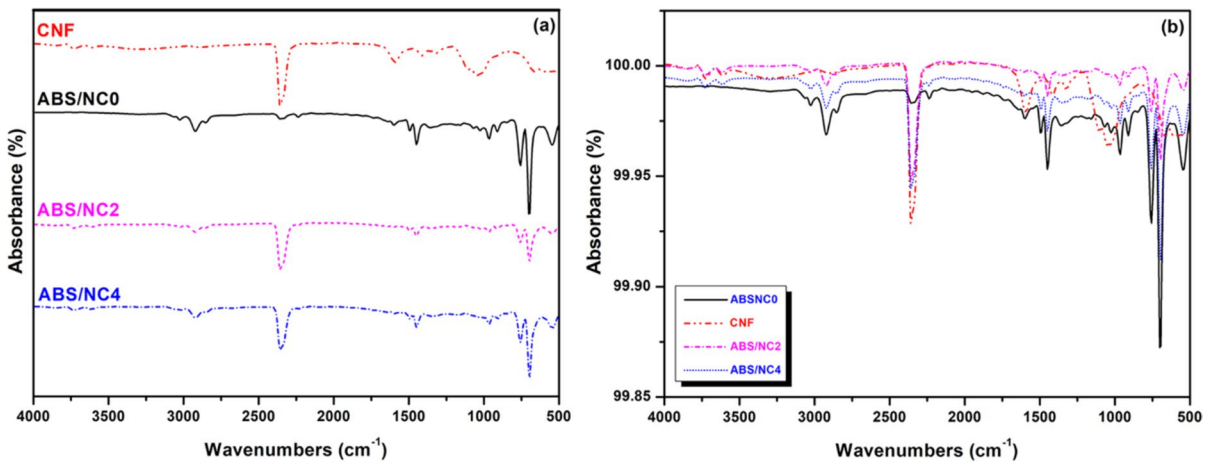

Fig. 6 Graphical comparison of FT-IR spectrum for ABS/CNF composites: **a** Singular display, **b** Overlapping display

In the FT-IR analysis of CNF, peaks in the range of 3734–3622 cm^{-1} overlap with the stretching vibrations of O–H single bonds (Rafi et al. 2023). The peak at 2357 cm^{-1} represents the stretching vibration of the carbonyl (C = O) group. The wave number 1592 cm^{-1} reflects the bending vibration of aromatic rings, while the peak at 1415 cm^{-1} corresponds to the stretching vibration of carbonyl (C-O) groups in the carbohydrate chains of cellulose. The peak at 1322 cm^{-1} indicates the presence of C-H bonds. The peak at 1104 cm^{-1} represents β-glycosidic bonds in cellulose, and the peak at 1049 cm^{-1} corresponds to the stretching vibration of carbonyl (C-O) groups in cellulose carbohydrate chains. The peak at 668 cm^{-1} represents the crystalline structures of cellulose (Soni and Mahmoud 2015; Wulandari et al. 2016; Tang and Jeong 2023; Osolnik et al. 2024).

In ABS/CNF composites, peaks belonging to both ABS and CNF are observed. Peaks at 3025, 2921, and 2852 cm^{-1} in the FT-IR results of ABS/CNF composites with 0.25% and 1% CNF content indicate the symmetric and asymmetric stretching vibrations of the methylene ($-CH_2$) group (Zhang et al. 2020; Qu et al. 2021; Afrin et al. 2022). The peak at 2357 cm^{-1} corresponds to the stretching vibration of the carbonyl (C = O) group, the peak at 2236 cm^{-1} corresponds to the stretching vibration of the nitrile (-CN) group, the peak at 1494 cm^{-1} corresponds to the bending vibration of the phenyl group, and the peak at 1449 cm^{-1} corresponds to the bending vibration of the aryl group. The peak at 1069 cm^{-1} indicates the presence of β-glycosidic bonds, while the peak at 1025 cm^{-1} corresponds to the bending vibration of the carbonyl (C = O) group. Outward bending vibrations of the phenyl ring of the styrene component are observed at 757 cm^{-1} and 696 cm^{-1}. Additionally, the peak at 544 cm^{-1} indicates the presence of cellulose crystalline structures (Soni and Mahmoud 2015; Wulandari et al. 2016; Tang and Jeong 2023; Osolnik et al. 2024).

DSC test results of ABS/CNF composites

The DSC curves depicted in Fig. 7 and the numerical data in Table 4 suggest that the presence of CNF in composite structures has a negligible impact on the Tg (glass transition temperature) and Tm (melting temperature) values. As observed in Fig. 7, the Tm peaks exhibit a single peak. Despite the inclusion of CNF, the existence of a solitary Tm peak implies that the ABS matrix can consistently absorb thermal energy even without the addition of CNF (Budiyantoro et al. 2019). The increases in Tg and Tm values in ABS/CNF composites are relatively marginal compared to pure ABS. For example, in pure ABS, Tg measured at 104.85 °C and Tm at 132.33 °C. The highest Tg and Tm values were recorded in the composite with a CNF addition ratio of 0.25, at 106.43 °C and 133.83 °C, respectively. This suggests that variations in Tm and Tg values may be contingent upon the distribution of CNF within the structure and the sampling region. Moreover, the elevated melting temperature in ABS/CNF composite could be ascribed to a higher concentration of CNF in the sampled region, acting partially as a nucleating agent, as melting temperature is known to be directly proportional to the size of the crystal nucleus (Araújo et al. 2010; Raimo 2015). These findings imply that the distribution of nanocellulose within the polymer matrix may partially influence the thermal properties of the composite material. Another notable observation from Table 4 is that both pure ABS and ABS/CNF composites exhibit negative enthalpy (ΔH) values, indicating an exothermic reaction. In comparison to pure ABS, the melting enthalpy of ABS/CNF composites (exothermic reaction) suggests its susceptibility to the presence of CNF. As previously mentioned, the variations in Tm and Tg values may generally hinge on the distribution of CNF within the structure and the sampling region.

TGA test results of ABS/CNF composites

The numerical data for pure ABS and ABS/CNF composites' TGA tests are provided in Table 5, TG curves in Fig. 8a, and DTG curves in Fig. 8b. Decomposition of pure ABS and ABS/CNF composites under nitrogen occurs approximately in a single stage around 340–500 °C, as observed in Fig. 8a. Some weight loss occurs in all samples up to the temperature where thermal degradation begins, attributed to moisture and volatile components in the material. The main decomposition of pure ABS and ABS/CNF composites is believed to occur with the degradation of butadiene monomer around 340–350 °C, styrene around 420 °C, and acrylonitrile between 400 and 450 °C (Suzuki and Wilkie 1995). Except for the ABS/CNF composite with 1% nanocellulose addition,

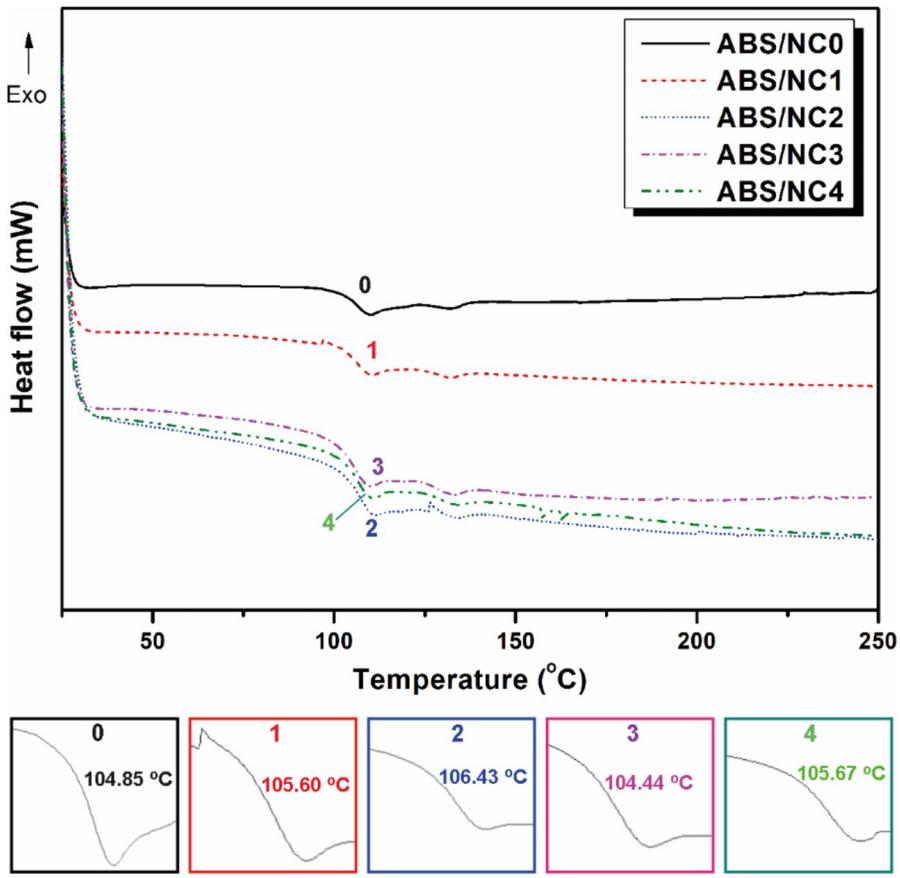

Fig. 7 DSC curves of ABS/CNF composites

Table 4 The numerical data obtained from the DSC test

Sample code	ΔH (J/g)	Tg (°C)	Tm (°C)
ABS/NC0	− 0.44	104.85	132.33
ABS/NC1	− 0.47	105.60	132.00
ABS/NC2	− 0.39	106.43	133.83
ABS/NC3	− 0.52	104.44	132.33
ABS/NC4	− 0.48	105.67	133.67

Table 5 The numerical data obtained from the TGA test

Sample code	T_5 (°C)	T_{50} (°C)	T_{max} (°C)	Residue at 600 °C (%)
ABS/NC0	396.7	425.7	471.6	1.9
ABS/NC1	395.7	466.0	427.6	2.1
ABS/NC2	395.9	426.9	470.2	1.3
ABS/NC3	394.5	426.0	468.8	1.6
ABS/NC4	380.0	415.7	455.3	2.9

T5 temperatures of all other samples are close to each other, indicating the onset of thermal degradation at similar temperature values. The highest T50 temperature is measured as 466 °C in the ABS/CNF composite coded with 0.125% CNF addition. The highest decomposition temperature (Tmax) is measured as 471.6 °C in pure ABS, consistent with literature values (Ma et al. 2007). In ABS/CNF composites, the lowest Tmax temperature is measured as 427.6 °C in the composite with 0.125% CNF addition. It is observed that as Tmax temperature increases, the residue amount decreases. The lowest residue amount of 1.3% is obtained at Tmax temperature of 470.2 °C in the sample coded with ABS/NC2, while the highest residue amount of 2.9% is obtained at Tmax temperature of 470.2 °C in the sample coded with ABS/NC4. Two peaks are observed in the decomposition of CNF in ABS/CNF composites. The first minor peak represents the mass loss caused by residual moisture evaporation, defined in the initial part of DTG

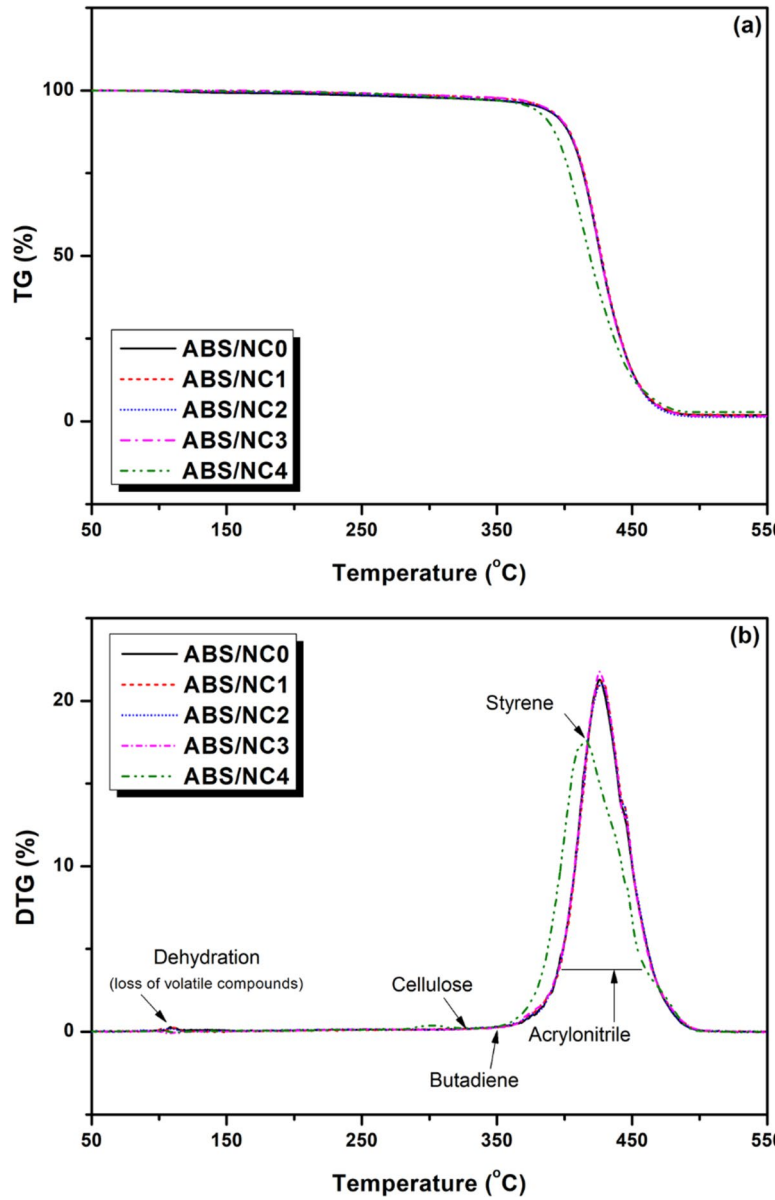

Fig. 8 TGA curves of ABS/CNF composites **a** TG and **b** DTG

curves, while the second peak mainly represents the main mass loss stage (a continuous stage) (Peng et al. 2013). This second peak continues from the temperature where thermal degradation begins to the end of the TGA test at the final test temperature of 600 °C.

SEM microstructure imaging results of ABS/CNF composites

The SEM image of CNFs is provided in Fig. 9. It clearly demonstrates that cellulose nanofibrils form a regular and longitudinal structure. The formation of long and thin fibrils results in a large surface area, and due to the possibly high density of hydroxyl groups on the fibril surface, fiber bundles interact strongly (Lee et al. 2009). This condition leads to a tendency

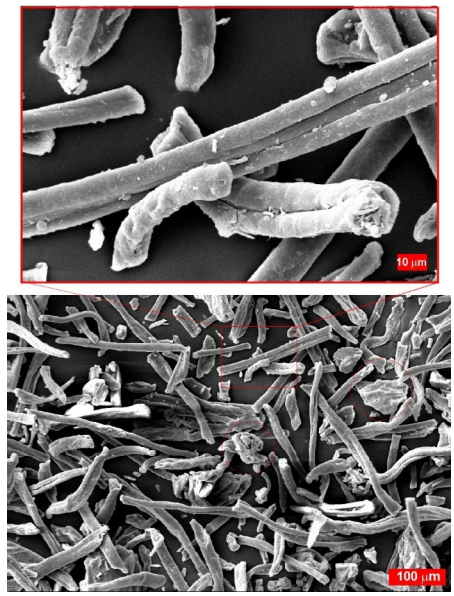

Fig. 9 SEM microstructure images of CNF

for agglomeration, as indicated within the red circle in Fig. 9.

The SEM images of fracture surfaces of ABS/CNF composites after notch less (Fig. 10a) and notched (Fig. 10b) impact tests are shown in Fig. 10. It can be observed that pure ABS (ABS/NC0) exhibit a smooth fracture surface. The addition of CNFs results a slight increase in surface roughness of ABS/CNF composites compared to pure ABS. SEM images generally indicate that CNFs are uniformly distributed within the ABS matrix. Particularly, the increase in CNF content confirms the enhancement of crack resistance. The fracture geometries and behaviors of ABS/NC0 and ABS/NC1 are similar. ABS/NC2 and ABS/NC3 composites exhibit higher resistance to fracture due to their elongated fracture surfaces. The shorter fracture surfaces observed in ABS/NC4 indicate rapid crack propagation, which might be attributed to an increase in agglomeration tendency or partially crystalline behavior with increasing CNF content (Lee et al. 2009; Kaushik et al. 2010). Additionally, ABS/NC4 shows more void and cavity formation compared to other composites. This is believed to create areas for crack initiation, leading to localized stress concentration (Ponsuriyaprakash et al. 2022). The presence of voids in the structure also suggests weak interfacial adhesion between the filler and the matrix, possibly due to agglomeration. The drop in impact test results confirms this situation.

Conclusion

A comprehensive analysis of the experimental data and characterization results reveals several key conclusions about the behavior and properties of ABS/CNF composites. The addition of CNFs to ABS composites enhances mechanical properties, particularly tensile strength and flexural strength, with ABS/NC4 (1% CNFs) showing the highest tensile modulus at 1013 ± 14 MPa and ABS/NC1 (0.125% CNFs) showing the highest flexural strength at 101.5 ± 1.20 MPa. However, increased CNF content reduces elongation at break, indicating a trade-off between stiffness and ductility. Impact resistance improves with CNF, peaking with ABS/NC2 (0.25% CNFs), where unnotched impact resistance is 90.63 kJ/m^2 and notched impact resistance is 23.22 kJ/m^2. Higher contents (0.5%) lead to a decline in impact resistance due to reduced homogeneity and microcrack formation. CNFs have a negligible impact on glass transition (Tg) and melting (Tm) temperatures, but slight variations suggest a potential influence of CNF distribution. Thermal degradation patterns are similar between pure ABS and ABS/CNF composites, with minor differences in decomposition temperature and residue amounts. SEM imaging shows uniform CNF distribution within the ABS matrix, enhancing crack resistance, but higher CNF content in ABS/NC4 leads to voids and cavities, indicating weak interfacial adhesion. Higher CNF content also improves surface gloss, indicating smoother surfaces. Overall, CNF incorporation into ABS composites enhances mechanical properties, impact resistance, and surface quality. However, careful optimization of CNF content and distribution is crucial to balance these improvements with other properties like ductility and surface quality, paving the way for advanced composites with tailored properties for specific applications, such as automotive (interior trim parts, bumpers, and paneling), consumer products where aesthetics and durability are crucial (such as sports equipment, furniture, and home appliances), and the electronics industry (for enclosures and structural components).

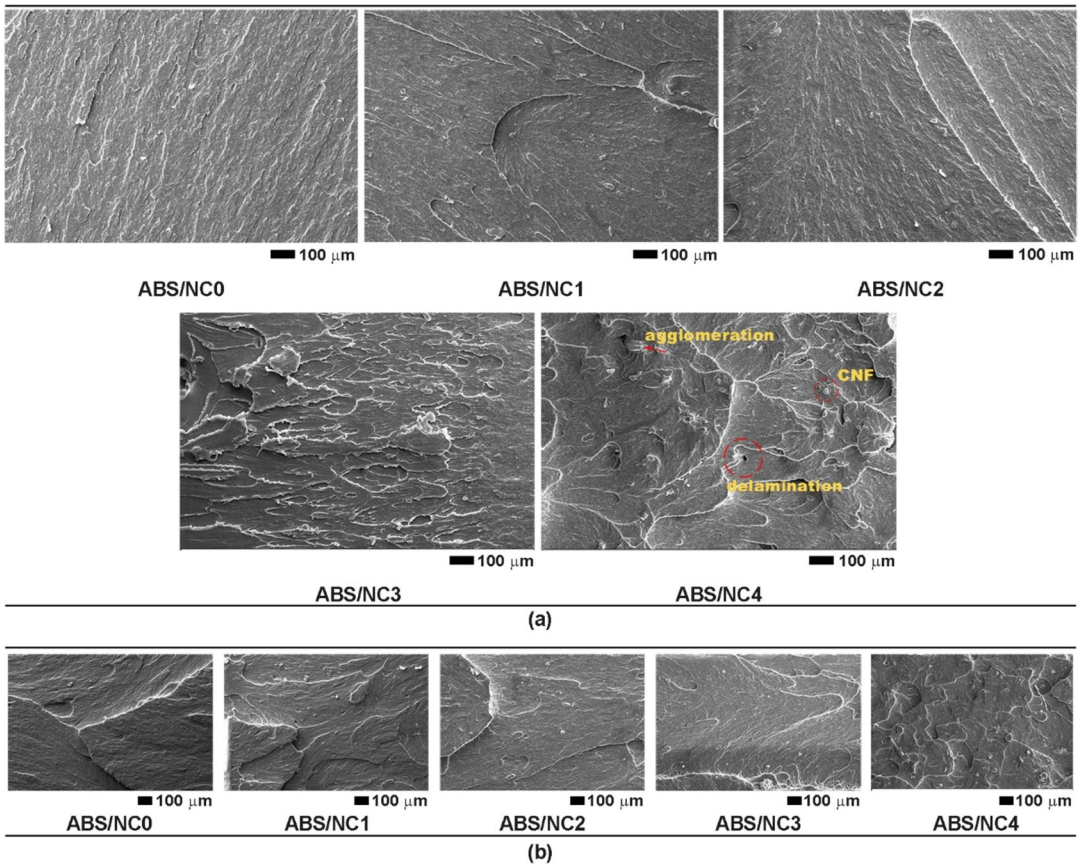

Fig. 10 SEM microstructure images of ABS/CNF composites: **a** Fracture surface SEM images of unnotched impact test, **b** Fracture surface SEM images of notched impact test

Acknowledgments The author gratefully acknowledges the financial support (Project No:23201096) of Selcuk University Scientific Research Projects Coordination Unit.

Author contributions The determination of the parameters, interpretation of the results, and writing of the article were carried out by İdris Karagöz and Harun Sepetçioğlu. The samples were prepared by Sultan Çavdar, İdris Karagöz and Harun Sepetçioğlu. Mechanical tests were conducted by Harun Sepetçioğlu, and thermal tests were performed by İdris Karagöz. All authors contributed to the writing of the article and the interpretation of the results.

Funding The author gratefully acknowledges the financial support (Project No:23201096) of Selcuk University Scientific Research Projects Coordination Unit.

Data Availability No datasets were generated or analysed during the current study.

Declarations

Conflict of interests The authors have no relevant financial or non-financial interests to disclose.

Ethics approval Not applicable.

References

Afrin S, Rahman MM, Akbor MA, Siddique MAB, Uddin MK, Malafaia G (2022) Is there tea complemented with the appealing flavor of microplastics? A pioneering study on plastic pollution in commercially available tea bags in Bangladesh. Sci Total Environ 837:155833

Araújo AAS, Bezerra MDS, Storpirtis S, Matos JDR (2010) Determination of the melting temperature, heat of fusion, and purity analysis of different samples of zidovudine (AZT) using DSC. Braz J Pharm Sci 46:37–43

Boldizar A, Klason C, Kubat J, Näslund P, Saha P (1987) Prehydrolyzed cellulose as reinforcing filler for thermoplastics. Int J Polym Mater 11(4):229–262

Bose S, Bhattacharyya AR, Häußler L, Pötschke P (2009) Influence of multiwall carbon nanotubes on the mechanical properties and unusual crystallization behavior in melt-mixed co-continuous blends of polyamide6 and acrylonitrile butadiene styrene. Polym Eng Sci 49(8):1533–1543

Boufi S, Kaddami H, Dufresne A (2014) Mechanical performance and transparency of nanocellulose reinforced polymer nanocomposites. Macromol Mater Eng 299(5):560–568

Budiyantoro C, Sosiati H, Nugroho A, Anggariawan A (2019) Thermal Characterization of Mixed Virgin-Recycle Acrylonitrile Butadiene Styrene. J Mate Dan Proses Manufaktur 3(2):83–89

Díaz de León R, Guzmán E, López González R, Díaz Elizondo A, Magaña I, Facio NG, Valencia L (2021) Surface modification of cellulose nanocrystals with lactone monomers via plasma-induced polymerization and their application in ABS nanocomposites. Polymers 13(16):2699

Farooq A, Patoary MK, Zhang M, Mussana H, Li M, Naeem MA, Mushtaq A, Farooq A, Liu L (2020) Cellulose from sources to nanocellulose and an overview of synthesis and properties of nanocellulose/zinc oxide nanocomposite materials. Int J Biol Macromol 154:1050–1073

Favier V, Canova GR, Cavaillé JY, Chanzy H, Dufresne A, Gauthier C (1995a) Nanocomposite materials from latex and cellulose whiskers. Polym Adv Technol 6(5):351–355

Favier V, Chanzy H, Cavaillé J (1995b) Polymer nanocomposites reinforced by cellulose whiskers. Macromolecules 28(18):6365–6367

Feng X, Yang Z, Rostom SS, Dadmun M, Xie Y, Wang S (2017) Structural, mechanical, and thermal properties of 3D printed L-CNC/acrylonitrile butadiene styrene nanocomposites. J App Polym Sci 134(31):45082

Guo R, Zhang L, Lu Y, Zhang X, Yang D (2020) Research progress of nanocellulose for electrochemical energy storage: A review. J Energy Chem 51:342–361

Jenol MA, Norrrahim MNF, Nurazzi NM (2022) Nanocellulose nanocomposites in textiles. industrial applications of nanocellulose and Its nanocomposites. Elsevier, Amsterdam, pp 397–408

Karagöz İ (2024) Production and characterization of sustainable biocompatible PLA/walnut shell composite materials. Polym Bullet. https://doi.org/10.1007/s00289-024-05247-4

Karagöz İ, Mutlu D, Çavuşoğlu A, Çelebi M, Ceylan Ö (2024) A comprehensive study on the effect of small rates of walnut shell and talc fillers on the thermal, mechanical, and morphological properties of epoxy hybrid composites. Biomass Convers Biorefin. https://doi.org/10.1007/s13399-024-05660-9

Kargarzadeh H, Mariano M, Huang J, Lin N, Ahmad I, Dufresne A, Thomas S (2017) Recent developments on nanocellulose reinforced polymer nanocomposites: a review. Polymer 132:368–393

Kargarzadeh H, Huang J, Lin N, Ahmad I, Mariano M, Dufresne A, Thomas S, Gałęski A (2018) Recent developments in nanocellulose-based biodegradable polymers, thermoplastic polymers, and porous nanocomposites. Prog Polym Sci 87:197–227

Katagiri K, Kishimoto N, Yamaguchi H, Okumura T, Kawakita S, Honda S, Sasaki K (2023) Effects of stacking sequences of non-hydrophobic cellulose nanofiber dispersion layer on impact properties of carbon fiber/cellulose nanofiber reinforced epoxy composite. Mechan Adv Mater Struct 30(3):582–591

Kaushik A, Singh M, Verma G (2010) Green nanocomposites based on thermoplastic starch and steam exploded cellulose nanofibrils from wheat straw. Carbohydr Polym 82(2):337–345

Kim CH, Youn HJ, Lee HL (2015) Preparation of cross-linked cellulose nanofibril aerogel with water absorbency and shape recovery. Cellulose 22:3715–3724

Leao RM, Jesus LC, Bertuoli PT, Zattera AJ, Maia JM, del Menezzi CHS, Amico SC, da Luz SM (2020) Production and characterization of cellulose nanocrystals/acrylonitrile butadiene styrene nanocomposites. J Compos Mater 54(27):4207–4214

Lee SY, Chun SJ, Kang IA, Park JY (2009) Preparation of cellulose nanofibrils by high-pressure homogenizer and cellulose-based composite films. J Ind Eng Chem 15(1):50–55

Lee KY, Aitomäki Y, Berglund LA, Oksman K, Bismarck A (2014) On the use of nanocellulose as reinforcement in polymer matrix composites. Compos Sci Technol 105:15–27

Ma H, Tong L, Xu Z, Fang Z, Jin Y, Lu F (2007) A novel intumescent flame retardant: Synthesis and application in ABS copolymer. Polym Degrad Stab 92(4):720–726

Ma L, Zhang Y, Meng Y, Anusonti-Inthra P, Wang S (2015) Preparing cellulose nanocrystal/acrylonitrile-butadiene-styrene nanocomposites using the master-batch method. Carbohydr Polym 125:352–359

Ma L, Zhang Y, Wang S (2017) Preparation and characterization of acrylonitrile-butadiene-styrene nanocomposites reinforced with cellulose nanocrystal via solution casting method. Polym Compos 38:E167–E173

Misenan MSM, Akhlisah ZN, Shaffie AH, Saad MAM, Norrahim MNF (2022) Nanocellulose in sensors. Ind App Nanocellul Nanocompos, 213–243

Moon RJ, Martini A, Nairn J, Simonsen J, Youngblood J (2011) Cellulose nanomaterials review: structure, properties and nanocomposites. Chem Soc Rev 40(7):3941–3994

Mutlu D, Karagöz İ, Sepetcioglu H, Tarim UA, Gurler O (2024) Synergizing electrical, mechanical, and radiation shielding properties of dendritic copper filled epoxy polymer composites. Radiat Phys Chem 216:111416

Osolnik U, Vek V, Korošec RC, Oven P, Poljanšek I (2024) Integration of wood-based components–cellulose nanofibrils and tannic acid-into a poly (vinyl alcohol) matrix to improve functional properties. Int J Biol Macromol 256:128495

Ozcan A, Tozluoglu A, Arman Kandirmaz E, Tutus A, Fidan H (2021) Printability of variative nanocellulose derived papers. Cellulose 28:5019–5031

Peng Y, Gardner DJ, Han Y, Kiziltas A, Cai Z, Tshabalala MA (2013) Influence of drying method on the material properties of nanocellulose I: thermostability and crystallinity. Cellulose 20:2379–2392

Ponsuriyaprakash S, Udhayakumar P, Pandiyarajan R (2022) Mechanical characterization and morphological behavior

of a novel composite of ABS polymer strengthened by cellulose. J Chin Inst Eng 45(3):255–265
Qu YH, Li YP, Zou XT, Xu KW, Xue YT (2021) Microwave treatment combined with wetting agent for an efficient flotation separation of acrylonitrile butadiene styrene (ABS) from plastic mixtures. J Mater Cycles Waste Manag 23:96–106
Rafi AA, Alimohammadzadeh R, Avella A, Mõistlik T, Jűrisoo M, Kaaver A, Tai CW, Re GL, Cordova A (2023) A facile route for concurrent fabrication and surface selective functionalization of cellulose nanofibers by lactic acid mediated catalysis. Sci Rep 13(1):14730
Raimo M (2015) Growth of spherulites: foundation of the DSC analysis of solidification. ChemTexts. https://doi.org/10.1007/s40828-015-0013-1
Saba N, Mohammad F, Pervaiz M, Jawaid M, Alothman OY, Sain M (2017) Mechanical, morphological and structural properties of cellulose nanofibers reinforced epoxy composites. Int J Biol Macromol 97:190–200
Siró I, Plackett D (2010) Microfibrillated cellulose and new nanocomposite materials: a review. Cellulose 17:459–494
Soni B, Mahmoud B (2015) Chemical isolation and characterization of different cellulose nanofibers from cotton stalks. Carbohydr Polym 134:581–589
Souza SF, Ferreira FV, Cherian BM, Silva VR, Manzato L, Pinheiro IF (2020) Processing of nanocellulose-based composites. Fiber-Reinforced Nanocomposites: Fundamentals and Applications. Elsevier, Amsterdam, pp 431–448
Spagnuolo L, D'Orsi R, Operamolla A (2022) Nanocellulose for paper and textile coating: the importance of surface chemistry. Chem plus Chem 87(8):e202200204
Suzuki M, Wilkie CA (1995) The thermal degradation of acrylonitrile-butadiene-styrene terpolymei as studied by TGA/FTIR. Polym Degrad Stab 47(2):217–221
Tang F, Jeong YG (2023) Interface-engineered polypropylene/cellulose nanofibril composites with enhanced thermal stability, mechanical modulus, and impact strength. Polym Compos 44(1):190–201
Tozluoglu A, Ates S, Durmaz E, Sertkaya S, Arslan R, Ozcelik O, Candan Z (2022) Nanocellulose in paper and board coating. Emerging nanomaterials: Opportunities and challenges in forestry sectors. Springer, Cham, Switzerland, pp 197–298
Wang J, Han X, Zhang C, Liu K, Duan G (2022) Source of nanocellulose and its application in nanocomposite packaging material: A review. Nanomaterials 12(18):3158
Wulandari WT, Rochliadi A, Arcana IM (2016) Nanocellulose prepared by acid hydrolysis of isolated cellulose from sugarcane bagasse. In IOP conference series: Mater Sci Eng 107(1):012045
Yang HS, Gardner DJ (2011) Mechanical properties of cellulose nanofibril-filled polypropylene composites. Wood Fiber Sci 43(2):143–152
Zaaba N, Zaaba F, Jaafar M, Ismail H (2021) Tensile and morphological properties of nanocrystalline cellulose and nanofibrillated cellulose reinforced PLA bionanocomposites: a review. Polym Eng Sci 61(1):22–38
Zhang Y, Jiang H, Wang H, Wang C (2020) Separation of hazardous polyvinyl chloride from waste plastics by flotation assisted with surface modification of ammonium persulfate: Process and mechanism. J Hazard Mater 389:121918
Zhang W, Zhang Y, Cao J, Jiang W (2021) Improving the performance of edible food packaging films by using nanocellulose as an additive. Int J Biol Macromol 166:288–296